

Two flavors of dynamical quarks on anisotropic lattices

T. Umeda*,¹ S. Aoki,² M. Fukugita,³ K.-I. Ishikawa,¹ N. Ishizuka,^{1,2} Y. Iwasaki,^{1,2} K. Kanaya,² Y. Kuramashi,⁴ V.I. Lesk,¹ Y. Namekawa,² M. Okawa,⁵ Y. Taniguchi,² A. Ukawa,^{1,2} and T. Yoshié,^{1,2}

(CP-PACS Collaboration)

¹*Center for Computational Physics, University of Tsukuba, Tsukuba, Ibaraki 305-8577, Japan*

²*Institute of Physics, University of Tsukuba, Tsukuba, Ibaraki 305-8571, Japan*

³*Institute for Cosmic Ray Research, University of Tokyo, Kashiwa, Chiba 277-8582, Japan*

⁴*High Energy Accelerator Research Organization (KEK), Tsukuba, Ibaraki 305-0801, Japan*

⁵*Department of Physics, Hiroshima University, Higashi-Hiroshima, Hiroshima 739-8526, Japan*

(Dated: November 6, 2018)

We report on our study of two-flavor full QCD on anisotropic lattices using $O(a)$ -improved Wilson quarks coupled with an RG-improved glue. The bare gauge and quark anisotropies corresponding to the renormalized anisotropy $\xi = a_s/a_t = 2$ are determined as functions of β and κ , which covers the region of spatial lattice spacings $a_s \approx 0.28\text{--}0.16$ fm and $m_{PS}/m_V \approx 0.6\text{--}0.9$. The calibrations of the bare anisotropies are performed with the Wilson loop and the meson dispersion relation at 4 lattice cutoffs and 5–6 quark masses. Using the calibration results we calculate the meson mass spectrum and the Sommer scale r_0 . We confirm that the values of r_0 calculated for the calibration using pseudo scalar and vector meson energy momentum dispersion relation coincide in the continuum limit within errors. This work serves to lay ground toward studies of heavy quark systems and thermodynamics of QCD including the extraction of the equation of state in the continuum limit using Wilson-type quark actions.

PACS numbers: 12.38.Gc

I. INTRODUCTION

In spite of recent progress in computer technology and numerical algorithms, extraction of continuum properties from lattice QCD remains to be challenging when dynamical quarks are included due to large computational demands. One of methods for alleviating the difficulty is to improve the lattice action for a faster approach to the continuum limit. This has enabled us to carry out the first systematic extrapolation to the chiral and continuum limits for the light hadron spectrum [1, 2].

Another method which is effective for several quantities is to introduce a space-time anisotropy. In Ref. [3], we have shown that using anisotropic lattices with a larger temporal cutoff is efficient for reducing lattice artifacts in thermal QCD, and have carried out the first well-controlled continuum extrapolation of the equation of state in quenched QCD. In finite temperature QCD, anisotropic lattices have been employed in the quenched approximation also to study transport coefficients [4], pole masses [5, 6], glueballs [7], and spectral functions [8, 9], where anisotropy was introduced to obtain more data points for temporal correlation functions. At zero temperature, anisotropic lattices have been employed to study charmonium states [10, 11, 12], glueballs [15], heavy hybrids [13, 14], and also the pion scattering length [16].

In this paper, we calculate the anisotropy parameters

for an improved full QCD action to contribute toward a systematic study of QCD with heavy quarks and at finite temperatures. The calculation of anisotropy parameters is not a simple task in full QCD because a couple of bare parameters have to be simultaneously adjusted to achieve a consistent renormalized anisotropy in physical observables for both quarks and gluons. This tuning of bare anisotropy parameters is called “calibration” [17]. We study two-flavor full QCD with an RG-improved gauge action and a clover-improved Wilson quark action, extending the combination of improved actions adopted by the CP-PACS Collaboration to anisotropic lattices. Carrying out simulations at several values of bare parameters, we perform the calibration to determine the bare anisotropy parameters for a given value of the renormalized anisotropy $\xi = a_s/a_t$ as functions of the gauge coupling and bare quark mass. We study the range of parameters corresponding to $a_s \approx 0.28\text{--}0.16$ fm for the spatial lattice spacing and $m_{PS}/m_V \approx 0.6\text{--}0.9$ for the ratio of pseudoscalar and vector meson masses. Based on our previous study of finite temperature QCD [3], we concentrate on the case $\xi = 2$ in this paper.

Different choices of observables for the calibration will lead to $O(a)$ differences in the calibration results. We study this issue by comparing the results from two different observables — pseudoscalar and vector meson dispersion relations. We anticipate that the results of different calibrations will be useful for checking the stability of continuum extrapolations. As a test of the idea, we also perform a continuum extrapolation of the Sommer scale at $\xi = 2$, by interpolating our measurement results to the calibrated points.

This paper is organized as follows: We define our

*Address after Apr. 2003: YITP, Kyoto University, Kyoto 606-8502, Japan.

anisotropic lattice action in Sec. II, and discuss our choice of $\xi = 2$ and simulation parameters in Sec. III. The calibration procedure is described in Sec. IV. Results of two calibrations for $\xi = 2$, using pseudoscalar and vector meson dispersion relations, are summarized in Sec. V. Finally, in Sect. VI, we interpolate the measurement results to $\xi = 2$ to study basic properties of our lattices. We also test how the difference in the calibration affects physical observables. Sec. VII is devoted to conclusions and discussions. An appendix is added to compare our calibration procedure with another method based on the ratio of screening and temporal masses.

II. ANISOTROPIC LATTICE ACTION

We study full QCD with two flavors of degenerate light quarks. On isotropic lattices, we have made a series of systematic studies adopting a clover-improved quark action coupled with an RG-improved glue [1, 2, 18, 19, 20, 21, 22]. In these studies, the clover coefficient c_{SW} was set to the tadpole-improved value using the plaquette in one-loop perturbation theory for the mean-field. This choice was based on the observations that the one-loop plaquette reproduces the actual plaquette expectation values within 8% for the range of parameters studied, and that the resulting value of the clover coefficient agrees well with actual one-loop value of it. This action was shown to give both a good rotational symmetry of the heavy quark potential and a small scale violations in the light hadron spectra at moderate lattice spacings [23]. At zero temperature, these good properties enabled us to carry out first systematic chiral and continuum extrapolations of light hadron spectra and light quark masses [1, 2]. At finite temperatures, this combination of actions was shown to reproduce the expected O(4) scaling around the two-flavor chiral transition point [18, 24], and was adopted in the first systematic calculation of the equation of state in lattice QCD with Wilson-type quarks [20]. Here, we extend the study to anisotropic lattices.

A. RG-improved gauge action on anisotropic lattice

On isotropic lattices, the RG-improved gauge action by Iwasaki [25] consists of plaquettes and 1×2 rectangular loops. Extending it to anisotropic lattices, the general form of the action is given by

$$S_G = \beta \left\{ \frac{1}{\gamma_G} \sum_{x,i>j} \{c_0^s P_{ij}(x) + c_1^s (R_{ij}(x) + R_{ji}(x))\} + \gamma_G \sum_{x,k} \{c_0^t P_{k4}(x) + c_1^t R_{k4}(x) + c_2^t R_{4k}(x)\} \right\}, \quad (1)$$

where i, j, k are for spatial directions and

$$P_{\mu\nu}(x) = 1 - \frac{1}{3} \text{ReTr} \{ U_\mu(x) U_\nu(x + \hat{\mu}) \times U_\mu^\dagger(x + \hat{\nu}) U_\nu^\dagger(x) \}, \quad (2)$$

$$R_{\mu\nu}(x) = 1 - \frac{1}{3} \text{ReTr} \{ U_\mu(x) U_\mu(x + \hat{\mu}) U_\nu(x + 2\hat{\mu}) \times U_\mu^\dagger(x + \hat{\mu} + \hat{\nu}) U_\nu^\dagger(x + \hat{\mu}) U_\nu^\dagger(x) \}, \quad (3)$$

are plaquette and rectangular loop in the μ - ν plane, respectively. The improvement coefficients $c_i^{s/t}$ satisfy the normalization conditions, $c_0^s + 8c_1^s = 1$ and $c_0^t + 4c_1^t + 4c_2^t = 1$. The bare gauge coupling equals $\beta = 6/g^2$, and γ_G represents the bare anisotropy. We have three independent improvement parameters among $c_i^{s/t}$.

In principle, these improvement coefficients may have non-trivial ξ dependences depending on the improvement conditions on the anisotropic lattice. In Ref. [26], we have repeated the improvement procedure of Iwasaki on anisotropic lattices, and found that, for small anisotropies $\xi \approx 1$ –4, the ξ -dependences in the improvement coefficients are weak, and a sufficient improvement is achieved just by fixing the coefficients to Iwasaki's values for isotropic lattices, $c_1^s = c_1^t = c_2^t = -0.331$. As explained in Sec. III, we are interested in the case $\xi = 2$. Because ξ -dependences in the improvement coefficients require additional elaborations in numerical simulations, such as computation of ξ -derivative terms in the equation of state (EOS), we fix the improvement coefficients to their isotropic values in the following.

B. Clover quark action on anisotropic lattice

We employ clover-improved Wilson quarks [27]. On anisotropic lattices, the action is given by

$$S_F = \sum_{x,y} \bar{q}(x) K(x,y) q(y), \quad (4)$$

$$K(x,y) = \delta_{x,y} - \kappa_t \left\{ (1 - \gamma_4) U_4(x) \delta_{x+\hat{4},y} + (1 + \gamma_4) U_4^\dagger(x - \hat{4}) \delta_{x-\hat{4},y} \right\} - \kappa_s \sum_i \left\{ (r - \gamma_i) U_i(x) \delta_{x+\hat{i},y} + (r + \gamma_i) U_i^\dagger(x - \hat{i}) \delta_{x-\hat{i},y} \right\} - \kappa_s \left\{ c_t \sum_i \sigma_{4i} F_{4i}(x) + r c_s \sum_{i>j} \sigma_{ij} F_{ij}(x) \right\} \delta_{x,y}. \quad (5)$$

For the field strength $F_{\mu\nu}$, we use the standard clover-leaf definition. Following our previous studies at $\xi = 1$, we apply a mean-field improvement for (4), $U_i(x) \rightarrow U_i(x)/u_s$ and $U_4(x) \rightarrow U_4(x)/u_t$, where u_s and u_t are mean links in the spatial and temporal directions. For the mean links, we adopt the value estimated from plaquette in one-loop perturbation theory as in our previous

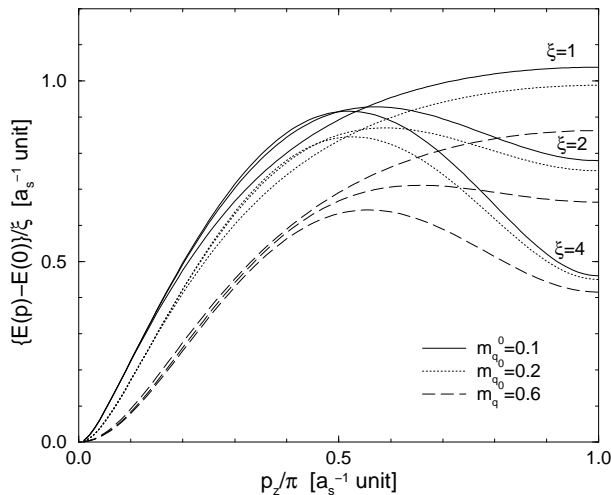


FIG. 1: Dispersion relation of free quark on anisotropic lattices. The energy $E(\vec{p}) - E(0)$ normalized by ξ is plotted as a function of spatial momentum at bare quark masses $m_q^0 = 0.1, 0.2$ and 0.6 (full, dotted and dashed curves) for anisotropies $\xi = 1, 2$ and 4 . Larger $E(\vec{p}) - E(0)/\xi$ at $p_z/\pi \sim 1$ correspond to smaller ξ .

studies. At $\xi = 2$, we obtain

$$W_{11}(ss) = 1 - 1.154/\beta, \quad (6)$$

$$W_{11}(st) = 1 - 0.560/\beta, \quad (7)$$

for spatial and temporal plaquettes. Therefore, we set $u_s = (1 - 1.154/\beta)^{1/4}$ for $\xi = 2$. For the temporal mean-field, we adopt $u_t = 1$ because a naively calculated value $W_{11}(st)^{1/2}/W_{11}(ss)^{1/4}$ exceeds 1 for $\xi \gtrsim 1.6$ at our values of β .

Following Refs. [5, 6], we set the spatial Wilson parameter to be $r = 1/\xi$. In this case, the quark dispersion relation in physical units preserves the 4-dimensional rotation symmetry at the tree level, and the tree-level improvement coefficients are free from the terms linear in m_q [12, 28, 29]. In a quenched study [30], it was shown that the fermionic bare anisotropy parameter corresponding to a fixed ξ is well fitted by a quadratic function of m_q with this choice of r . With dynamical quarks, however, terms linear in m_q may appear through quark loop corrections [29].

The clover coefficients, c_s and c_t , are functions of r . With our choice $r = 1/\xi$, c_s and c_t are unity at the tree level and their mean-field improved values are given by

$$c_t = \frac{1}{u_s u_t^2}, \quad c_s = \frac{1}{u_s^3}. \quad (8)$$

We define the bare anisotropy of the fermion field by

$$\gamma_F = \frac{\kappa_t u_t}{\kappa_s u_s}. \quad (9)$$

The bare quark mass in units of a_s is given by

$$m_q^0 = \frac{1}{2\kappa_s u_s} - \gamma_F - 3r. \quad (10)$$

For later convenience, we define κ which satisfy the same relation with m_q^0 as in the isotropic case:

$$\frac{1}{\kappa} = 2(m_q^0 + 4) = \frac{1}{\kappa_s u_s} - 2(\gamma_F + 3r - 4). \quad (11)$$

We perform chiral extrapolations in terms of $1/\kappa$.

The relation $r = 1/\xi$ suggests that spatial doublers may appear at large ξ . The free quark dispersion relation for our action is given by

$$\cosh E(\vec{p}) = 1 + \frac{\vec{p}^2 + \left(\frac{m_q^0}{\gamma_F} + \frac{r}{2\gamma_F} \hat{p}^2\right)^2}{2\left(1 + \frac{m_q^0}{\gamma_F} + \frac{r}{2\gamma_F} \hat{p}^2\right)}, \quad (12)$$

where $\vec{p}_i = (\sin p_i)/\gamma_F$, $\hat{p}_i = 2 \sin(p_i/2)$, and E is in units of a_t while p_i is in units of a_s [30]. In Fig. 1, we plot the energy $E(\vec{p})/\xi$ for $\xi = 1, 2$ and 4 at $m_q^0 = 0.1, 0.2$ and 0.6 , where $\xi = \gamma_F$ in this approximation. From this figure, we expect that doubler effects are weak at $\xi = 2$ and $m_q = (1/\kappa - 1/\kappa_c)/2 = 0.07\text{--}0.8$ we study (see Sec. VI).

III. SIMULATION PARAMETERS

In this paper, we focus on the case of the renormalized anisotropy $\xi = 2$. We have shown for finite-temperature pure SU(3) gauge theory [3] that this choice of ξ is optimal to reduce scaling violations in equation of state both in the high temperature limit and at finite β ; the latter is confirmed by a Monte Carlo simulation. It is straightforward to analyze the high temperature limit for full QCD. We have found that $\xi = 2$ is optimal also with two flavors of dynamical quarks and improved glue.

We perform simulations at $\beta = 1.8, 1.9, 2.0$, and 2.1 on $8^3 \times 24, 8^3 \times 24, 10^3 \times 30$ and $12^3 \times 36$ lattices, respectively. The lattice spacing is in the range $a_s \approx 0.28\text{--}0.16$ fm, and hence the spatial lattice size is fixed to be about 2 fm. See Sec. VI for details of the scale determination. At each β , six values of κ , corresponding to $m_{PS}/m_V \approx 0.6, 0.7, 0.8, 0.85, 0.9$, and 0.92 , are simulated. To study lattice volume effects, we also perform additional simulations on $8^3 \times 24$ and $12^3 \times 36$ lattices at $\beta = 2.0$. Our simulation parameters are summarized in Table I.

We generate gauge configurations by the HMC algorithm with an even-odd preconditioned BiCGStab quark solver [2]. The molecular dynamics time step dt is adjusted to achieve an acceptance rate of about 70–80%. Measurements are performed at every 5 trajectories over 1000–1700 trajectories after 300 thermalization trajectories, where the length of one trajectory is set to unity. Statistical errors of the observables are estimated by the jackknife method at each β and κ with bins of 50 trajectories.

TABLE I: Simulation parameters. “traj.” is the number of trajectories used for measurements after 300 thermalization trajectories. At $\beta = 2.0$, besides the main simulation on the $10^3 \times 30$ lattice, simulations using the same values of κ , γ_F , γ_G , and the trajectory length are done also on $8^3 \times 24$ and $12^3 \times 36$ lattices for a study of finite size effects.

β	size	κ	traj.	$(\gamma_G, \gamma_F u_s)$
1.8	$8^3 \times 24$	0.10745	1700	(1.70,0.90), (1.70,1.10), (1.70,1.20), (1.75,0.90), (1.75,1.10), (1.75,1.20), (1.85,0.90), (1.85,1.10)
		0.11162	1700	(1.70,1.00), (1.70,1.20), (1.70,1.30), (1.75,1.00), (1.75,1.20), (1.75,1.30)
		0.11582	1700	(1.70,1.15), (1.70,1.25), (1.70,1.30), (1.75,1.15), (1.75,1.25), (1.75,1.30)
		0.12115	1700	(1.70,1.25), (1.70,1.35), (1.70,1.40), (1.75,1.25), (1.75,1.35), (1.75,1.40)
		0.12438	1700	(1.70,1.20), (1.70,1.30), (1.70,1.40), (1.70,1.45), (1.75,1.30), (1.75,1.40), (1.75,1.45), (1.80,1.20)
		0.12655	1700	(1.70,1.35), (1.70,1.40), (1.70,1.45), (1.75,1.35), (1.75,1.40), (1.75,1.45)
1.9	$8^3 \times 24$	0.1085	1000	(1.80,1.00), (1.80,1.10), (1.80,1.20), (1.80,1.30), (1.85,1.00), (1.85,1.10), (1.85,1.20), (1.85,1.30),
		0.1137	1000	(1.80,1.15), (1.80,1.25), (1.80,1.35), (1.85,1.15), (1.85,1.25), (1.85,1.35)
		0.1169	1000	(1.75,1.20), (1.75,1.30), (1.75,1.40), (1.80,1.20), (1.80,1.30), (1.80,1.40), (1.85,1.20), (1.85,1.30)
		0.1212	1000	(1.75,1.55), (1.80,1.25), (1.80,1.35), (1.80,1.45), (1.80,1.55), (1.85,1.25), (1.85,1.35), (1.85,1.45)
		0.1245	1500	(1.70,1.50), (1.70,1.60), (1.75,1.30), (1.80,1.40), (1.80,1.50), (1.85,1.30), (1.85,1.60)
		0.1260	1500	(1.75,1.40), (1.75,1.60), (1.80,1.50), (1.85,1.40), (1.85,1.60), (1.90,1.50)
2.0	$10^3 \times 30$	0.1090	1000	(1.80,1.25), (1.80,1.35), (1.80,1.45), (1.85,1.25), (1.85,1.35)
	$(8^3 \times 24)$	0.1150	1000	(1.80,1.45), (1.80,1.55), (1.85,1.35), (1.85,1.45), (1.85,1.55), (1.95,1.45)
	$(12^3 \times 36)$	0.1180	1000	(1.80,1.40), (1.80,1.50), (1.80,1.60), (1.85,1.50), (1.85,1.60)
		0.1210	1000	(1.80,1.45), (1.80,1.55), (1.80,1.65), (1.85,1.45), (1.85,1.55), (1.95,1.45)
		0.1244	1500	(1.70,1.60), (1.80,1.50), (1.80,1.60), (1.80,1.70), (1.85,1.55), (1.85,1.60), (1.90,1.55), (1.90,1.60), (2.00,1.50)
		0.1252	1500	(1.75,1.60), (1.75,1.65), (1.80,1.60), (1.85,1.55), (1.85,1.65)
2.1	$12^3 \times 36$	0.1100	1000	(1.80,1.35), (1.80,1.55), (1.90,1.45), (1.95,1.35)
		0.1150	1000	(1.80,1.50), (1.80,1.60), (1.90,1.45), (1.90,1.55), (1.90,1.65)
		0.1200	1000	(1.80,1.65), (1.85,1.55), (1.90,1.75), (1.95,1.50), (1.95,1.60)
		0.1225	1500	(1.80,1.60), (1.80,1.70), (1.80,1.80), (1.90,1.60), (1.90,1.70), (1.90,1.80)
		0.1245	1500	(1.80,1.60), (1.80,1.80), (1.85,1.70), (1.90,1.60), (1.90,1.70)

IV. CALIBRATION PROCEDURE

At each β and κ , we have to tune the bare anisotropy parameters γ_F and γ_G such that the renormalized anisotropies ξ_F and ξ_G for fermionic and gluonic observables coincide with each other:

$$\xi_F(\gamma_F, \gamma_G; \beta, \kappa) = \xi_G(\gamma_F, \gamma_G; \beta, \kappa) = \xi. \quad (13)$$

As discussed in the previous section, we study the case $\xi = 2$. For this purpose, we measure ξ_F and ξ_G at several values of (γ_F, γ_G) at fixed κ and β , and determine the point where Eq. (13) is satisfied by an interpolation in γ_F and γ_G . Let us denote the resulting values of γ_F and γ_G for $\xi = 2$ as $\gamma_F^*(\beta, \kappa)$ and $\gamma_G^*(\beta, \kappa)$. Finally, we parametrize γ_F^* and γ_G^* as functions of β and κ for use in future studies of heavy quark systems and thermodynamics of QCD.

We measure ξ_G by Klassen’s method [10]:

$$R_s(x, y) = R_t(x, \xi_G y), \quad (14)$$

where

$$R_s(x, y) = \frac{W_{ss}(x, y)}{W_{ss}(x+1, y)}, \quad (15)$$

$$R_t(x, t) = \frac{W_{st}(x, t)}{W_{st}(x+1, t)}, \quad (16)$$

are the ratios of spatial-spatial and spatial-temporal Wilson loops, $W_{ss}(x, y)$ and $W_{st}(x, t)$, respectively. We determine ξ_G by minimizing

$$L(\xi_G) = \sum_{x,y} \frac{(R_s(x, y) - R_t(x, \xi_G y))^2}{(\Delta R_s)^2 + (\Delta R_t)^2}, \quad (17)$$

with ΔR_s and ΔR_t the statistical errors of R_s and R_t . To avoid short range lattice artifacts, x and y should not be too small. Practical range of x and y will be discussed later.

For ξ_F we use the relativistic dispersion relation of mesons:

$$E(\vec{p})^2 = m^2 + \frac{\vec{p}^2}{\xi_F^2} + O(\vec{p}^4), \quad (18)$$

where E and m are the energy and mass in units of a_t , and $\vec{p} = 2\pi\vec{n}/L_s$, with L_s the spatial lattice size, is the spatial momentum in units of a_s . We evaluate E and m from a cosh fit of the meson two-point correlation function,

$$C(\vec{p}, t) = \sum_{\vec{x}} \langle O(\vec{x}, t) O^\dagger(\vec{0}, 0) e^{i\vec{p}\vec{x}} \rangle \quad (19)$$

$$O(\vec{x}, t) = \sum_{\vec{y}\vec{z}} \phi(\vec{y}) \phi'(\vec{z}) \bar{q}(\vec{x} + \vec{y}, t) \Gamma q(\vec{x} + \vec{z}, t) \quad (20)$$

In this paper, we study pseudoscalar (PS) and vector (V) mesons consisting of sea quarks only: $\Gamma = \gamma_5$ for PS and $\Gamma = \gamma_i$ for V. Quark fields are smeared by a function $\phi(\vec{x})$ to enhance ground state signals at short distances. For the “smeared” quark field, we adopt an exponential smearing function of form

$$\phi(\vec{x}) = a \exp(-p|\vec{x}|) \text{ for } \vec{x} \neq 0, \quad \phi(\vec{0}) = 1, \quad (21)$$

where the coefficients a and p are adopted from a previous study [2]. The “point” quark field corresponds to $\phi(\vec{x}) = \delta_{\vec{x}, \vec{0}}$. In our calculation of meson two-point function, the sink operator is always the point-point type, while, for the source operator, we study point-point, point-smeared and smeared-smeared cases. We find that the smear-smear source operator leads to the earliest plateau with small errors. Therefore, we adopt the smear-smear source operator.

In principle, we may adopt different observables to define the renormalized anisotropies. Away from the continuum limit, different choices will lead to $O(a)$ differences in the calibration results. To study this problem, we compare the calibration results using ξ_F from PS and V meson dispersion relations. We denote these results for the calibrated bare anisotropies as $(\gamma_F^*(PS), \gamma_G^*(PS))$ and $(\gamma_F^*(V), \gamma_G^*(V))$, respectively. In Sec. VC, we show that they tend to converge together toward the continuum limit. In future applications of the present work, different sets of (γ_F^*, γ_G^*) will be useful for estimating systematic errors due to the continuum extrapolation, in complicated physical observables, such as the equation of state.

In a previous study of quenched QCD [5], the ratio of temporal and screening masses of the PS meson was used to determine ξ_F . We study the difference between our procedure and the mass ratio method in Appendix A. We find that both methods give consistent values of ξ_F when the quarks are not too heavy [$m_{PS}/m_V \lesssim 0.75$ (0.8) at $\beta \gtrsim 2.0$ (2.1)].

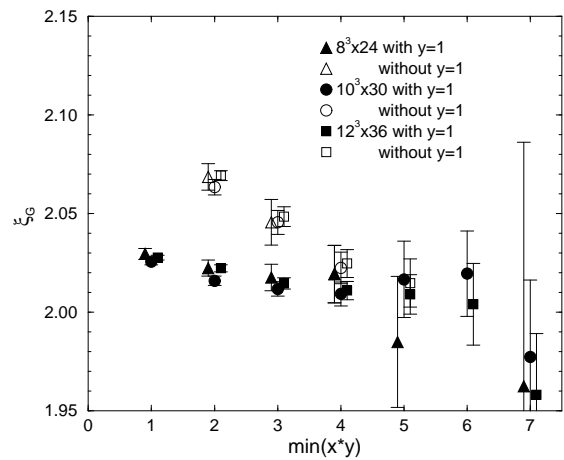


FIG. 2: A typical for a determination of ξ_G at $\beta = 2.0$, $\kappa = 0.1244$ and $(\gamma_G, \gamma_F u_s) = (1.85, 1.60)$. The ξ_G shows the minimizing point of $L(\xi_G)$ defined by Eq.17. Different symbols represent the results obtained on $8^3 \times 24$, $10^3 \times 30$ and $12^2 \times 36$ lattices. For filled/open symbols, $L(\xi_G)$ is evaluated with/without the $y = 1$ data.

V. CALIBRATION RESULTS

A. ξ_G from matching of Wilson loop ratios

We determine the renormalized gauge anisotropy ξ_G by minimizing the function $L(\xi_G)$ defined by Eq. (17). We interpolate $R_t(x, t)$ by a cubic spline in terms of t . To remove short range lattice artifacts, we evaluate $L(\xi_G)$ with x and y which satisfy $x \times y \geq M$ and examine the M dependence. The upper limit on x and y is set by requiring that the statistical error does not exceed the central value for the Wilson loop ratio. Varying the upper limit hardly changes results for ξ_G . Filled symbols in Fig. 2 show typical results of ξ_G as a function of $M = \min(x \times y)$. We find that, at this simulation point, ξ_G is reasonably stable when $x \times y$ is larger than about 4.

Since the condition $x \times y \geq M$ does not exclude small x or y , which can be an additional origin of short distance effects, we study whether ξ_G are affected by small values of x or y by removing them. The results of ξ_G using $L(\xi_G)$ without data at $y = 1$ are plotted with open symbols in Fig. 2. We find that, although clear deviations from the filled symbols are observed at small M , the effects of $y = 1$ data are within 1% at $M \gtrsim 4$ where ξ_G becomes stable. Therefore, placing a condition on $\min(x \times y)$ is sufficient to obtain a stable value for ξ_G . Similar results are obtained at other simulation points.

Results obtained on different lattice volumes ($8^3 \times 24$, $10^3 \times 30$ and $12^2 \times 36$) are also shown in Fig. 2. With our lattices, no finite volume effects are visible in the values of ξ_G .

From these studies, we adopt $\min(x \times y) = 3, 3, 4$, and 5 at $\beta = 1.8, 1.9, 2.0$ and 2.1, respectively, in the subsequent analyses.

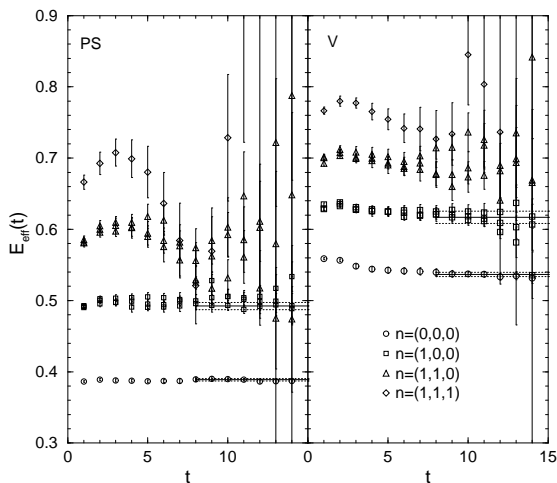


FIG. 3: Effective mass of meson states with various momenta obtained at $\beta = 2.0$, $\kappa = 0.1244$, $(\gamma_G, \gamma_{Fus}) = (1.85, 1.60)$ on the $10^3 \times 30$ lattice. The left and right panels are the results for pseudoscalar and vector mesons.

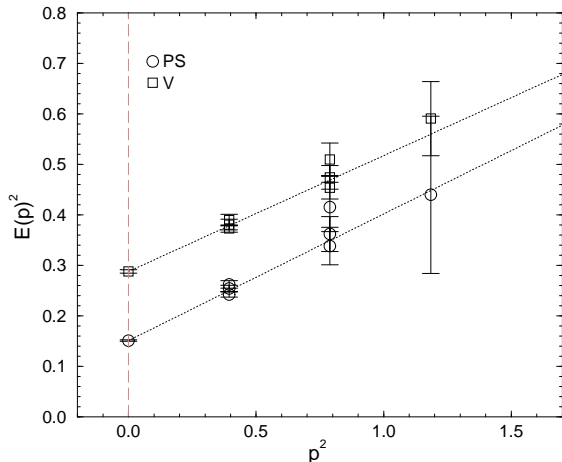


FIG. 4: Sample results for the dispersion relation of pseudoscalar and vector mesons at $\beta = 2.0$, $\kappa = 0.1244$ and $(\gamma_G, \gamma_{Fus}) = (1.85, 1.60)$. Dotted lines show fit results from $\vec{n} = (0, 0, 0)$ and $(1, 0, 0)$.

B. ξ_F from meson dispersion relations

We determine the renormalized quark anisotropy ξ_F from the meson dispersion relation. We calculate the meson energy $E(\vec{p})$ at the spatial momenta $\vec{p} = 2\pi\vec{n}/L_s$ with $\vec{n} = (0, 0, 0)$, $(1, 0, 0)$, $(1, 1, 0)$, $(1, 1, 1)$, and their permutations. In Fig. 3 we plot typical data for effective energy defined by

$$\frac{C(\vec{p}, t)}{C(\vec{p}, t+1)} = \frac{\cosh[E_{\text{eff}}(\vec{p}, t)(N_t/2 - t)]}{\cosh[E_{\text{eff}}(\vec{p}, t)(N_t/2 - t - 1)]}. \quad (22)$$

obtained from the smear-smear correlators. Typical results for the energy $E(\vec{p})$ are shown in Fig. 4.

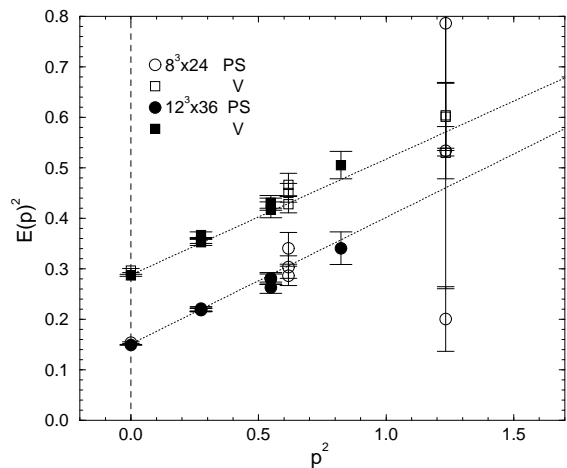


FIG. 5: Volume dependence of a mesonic dispersion relations at $\beta = 2.0$, $\kappa = 0.1244$ and $(\gamma_G, \gamma_{Fus}) = (1.85, 1.60)$. Filled and open symbols show the results on $12^3 \times 36$ and $8^3 \times 24$ lattices with PS and V channels. Other condition is same as Fig.4 and fit results on $10^3 \times 30$, which are the same as Fig.4, are shown with dotted lines.

Using data at $\vec{n} = (0, 0, 0)$, $(1, 0, 0)$ and its permutations, we fit $E(\vec{p})$ with the leading formula $E(\vec{p})^2 = m^2 + \vec{p}^2/\xi_F^2$ to determine ξ_F . The fits are shown by dotted lines in Fig. 4. In Fig. 5, data obtained on $8^3 \times 24$ and $12^3 \times 36$ lattices are compared with the fit results on the $10^3 \times 30$ lattice. We find that the data are well explained by the fit results. Indeed, the slope obtained for the three lattice sizes are consistent: $\xi_F = 2.044(59)$, $2.020(44)$ and $2.012(39)$ on $8^3 \times 24$, $10^3 \times 30$ and $12^3 \times 36$ lattices, respectively. This confirms that the spatial lattice size $\gtrsim 1.6$ fm is sufficiently large to suppress finite volume effects in ξ_F in the range of quark masses we study.

C. Bare anisotropies at $\xi = 2$ (γ_G^* and γ_F^*)

Figures 6–9 show typical results for bare anisotropies at each β , obtained at the third and fifth heaviest quark masses ($m_{PS}/m_V \sim 0.85$ and 0.70). We find that, for the range of parameters we study, we can fit the data assuming an ansatz linear in γ_F and γ_G :

$$\xi_F = a_F + b_F\gamma_F + c_F\gamma_G, \quad (23)$$

$$\xi_G = a_G + b_G\gamma_F + c_G\gamma_G. \quad (24)$$

Results of the least χ^2 fits are also shown in Figs. 6–9.

From the condition $\xi_F(\gamma_F^*, \gamma_G^*) = \xi_G(\gamma_F^*, \gamma_G^*) = 2$, we obtain γ_F^* and γ_G^* for $\xi = 2$ as functions of the coefficients, a_F, \dots, c_G . We determine their errors using the error propagation formula where the errors for a_F, \dots, c_G are estimated from the error matrix of the least χ^2 fits for ξ_F and ξ_G . The results are summarized in Table II.

To confirm the magnitude of errors, we study $\chi_{\text{total}}^2/N_{df} \equiv (\chi_{F;2}^2 + \chi_{G;2}^2)/2N_{df}$, as a function of γ_F and

TABLE II: Bare anisotropy parameters calibrated to $\xi = 2$.

β	κ	$\gamma_G^*(\text{PS})$	χ^2/N_{df}	$\gamma_F^*(\text{PS})$	χ^2/N_{df}	$\gamma_G^*(V)$	χ^2/N_{df}	$\gamma_F^*(V)$	χ^2/N_{df}
1.8	0.10745	1.742(11)	12.4/ 5	1.499(12)	6.7/ 5	1.7748(93)	12.4/ 5	1.2783(82)	3.1/ 5
	0.11162	1.734(12)	2.7/ 3	1.571(17)	2.6/ 3	1.740(18)	2.7/ 3	1.298(21)	2.0/ 3
	0.11582	1.725(11)	2.2/ 3	1.682(20)	1.2/ 3	1.768(20)	2.2/ 3	1.464(43)	2.4/ 3
	0.12115	1.7282(81)	0.9/ 3	1.784(11)	1.4/ 3	1.757(15)	0.9/ 3	1.613(14)	7.8/ 3
	0.12438	1.703(13)	2.1/ 5	1.879(16)	3.3/ 5	1.769(14)	2.1/ 5	1.676(28)	2.5/ 5
	0.12655	1.708(22)	1.1/ 3	1.895(15)	4.9/ 3	1.760(22)	1.1/ 3	1.786(13)	1.4/ 3
1.9	0.10850	1.8068(80)	1.6/ 5	1.554(12)	5.1/ 5	1.8093(56)	1.6/ 5	1.387(15)	5.8/ 5
	0.11370	1.7971(94)	2.9/ 3	1.675(12)	1.3/ 3	1.8126(60)	2.9/ 3	1.5615(84)	1.6/ 3
	0.11690	1.760(11)	1.3/ 5	1.753(13)	7.2/ 5	1.7945(74)	1.3/ 5	1.6085(82)	3.8/ 5
	0.12120	1.773(10)	4.0/ 5	1.858(13)	1.6/ 5	1.8013(75)	4.0/ 5	1.742(13)	7.3/ 5
	0.12450	1.7631(72)	2.1/ 4	1.927(13)	2.2/ 4	1.7908(85)	2.1/ 4	1.807(30)	1.5/ 4
	0.12600	1.7629(93)	2.8/ 3	1.987(17)	1.8/ 3	1.7811(77)	2.8/ 3	1.918(12)	4.9/ 3
2.0	0.10900	1.8243(40)	2.9/ 2	1.6931(70)	4.1/ 2	1.8319(38)	2.9/ 2	1.6266(95)	1.3/ 2
	0.11500	1.8288(52)	1.5/ 3	1.8015(85)	0.9/ 3	1.8331(76)	1.5/ 3	1.7190(98)	6.7/ 3
	0.11800	1.8243(65)	5.9/ 2	1.8907(74)	0.2/ 2	1.8315(88)	5.9/ 2	1.8268(83)	0.1/ 2
	0.12100	1.8225(73)	7.5/ 3	1.935(19)	3.3/ 3	1.8278(71)	7.5/ 3	1.903(25)	2.5/ 3
	0.12440	1.8120(73)	12.1/ 6	2.002(19)	1.7/ 6	1.8299(92)	12.1/ 6	1.938(27)	3.1/ 6
	0.12520	1.8169(76)	2.2/ 2	2.026(14)	0.4/ 2	1.8289(78)	2.2/ 2	1.949(58)	5.5/ 2
	2.1	0.11000	1.8814(88)	2.7/ 1	1.796(10)	1.4/ 1	1.8827(79)	2.7/ 1	1.760(11)
	0.11500	1.8678(70)	4.5/ 2	1.8932(74)	17.5/ 2	1.8722(73)	4.5/ 2	1.8501(85)	19.4/ 2
	0.12000	1.8673(87)	0.0/ 2	1.970(18)	1.2/ 2	1.871(16)	0.0/ 2	1.954(49)	0.6/ 2
	0.12250	1.8559(58)	2.6/ 3	2.032(23)	3.6/ 3	1.8603(62)	2.6/ 3	2.004(20)	6.0/ 3
	0.12450	1.8517(55)	1.6/ 2	2.043(14)	1.0/ 2	1.8615(68)	1.6/ 2	1.980(29)	4.8/ 2

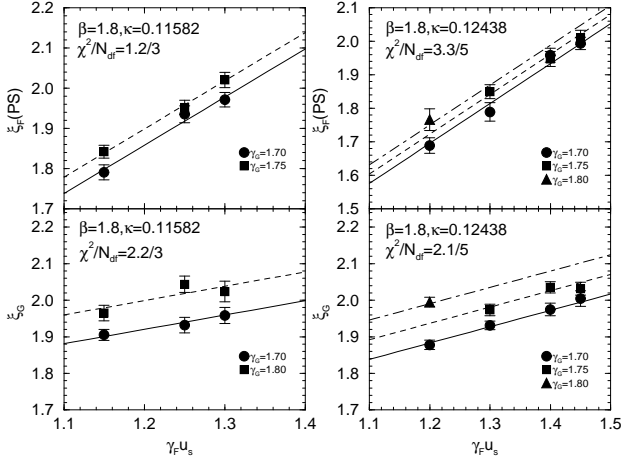


FIG. 6: ξ_G and ξ_F as functions of $(\gamma_G, \gamma_F u_s)$ at $\beta = 1.8$ for the third and fifth heaviest κ . For ξ_F , results from the pseudoscalar dispersion relation are shown. Lines represent the results of the fits (23) and (24).

γ_G , where $\chi_{F/G;2}^2$ is the χ^2 value for a fit of $\xi_{F/G}(\gamma'_F, \gamma'_G)$ data to $\xi_{F/G} = 2 + b(\gamma'_F - \gamma_F) + c(\gamma'_G - \gamma_G)$ for given values of (γ_F, γ_G) . This quantity measures to which extent $\xi = 2$ is achieved by Wilson loops and the meson correlation function at (γ_F, γ_G) . The minimum of χ_{total}^2/N_{df}

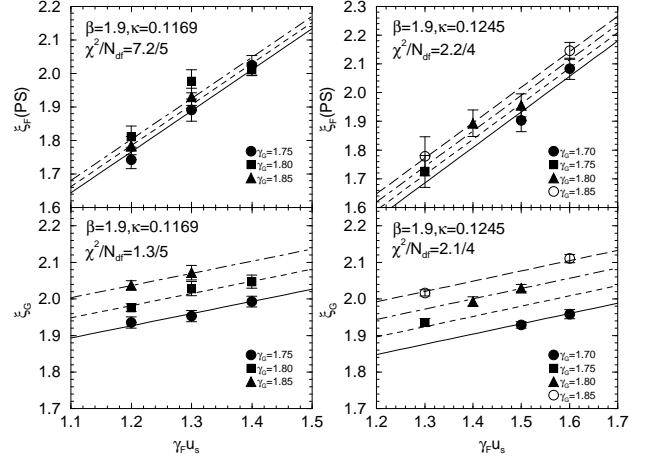
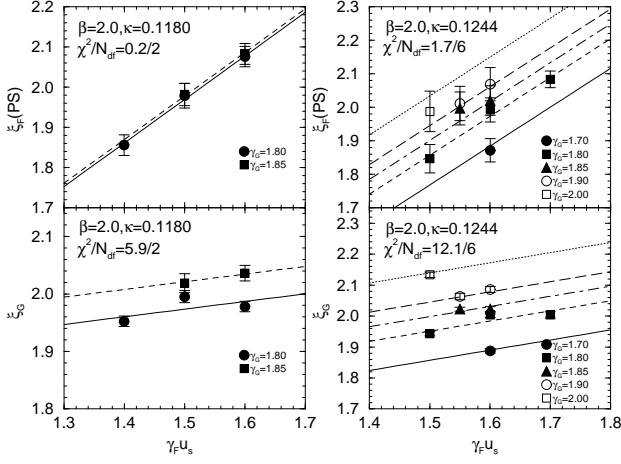
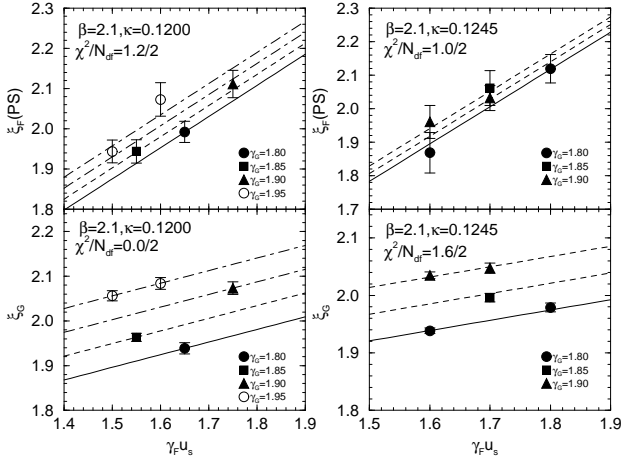


FIG. 7: The same as Fig. 6 but at $\beta = 1.9$.

locates at (γ_F^*, γ_G^*) . A typical result is plotted in Fig. 10. We find that errors estimated from a unit increase of χ_{total}^2/N_{df} are consistent with those listed in Table II.

In later applications, it will be convenient to parametrize γ_F^* and γ_G^* as functions of β and κ . Figures 11 and 12 show the parameter dependence of γ_F^* and γ_G^* . We adopt the general quadratic ansatz in β and

FIG. 8: The same as Fig. 6 but at $\beta = 2.0$.FIG. 9: The same as Fig. 6 but at $\beta = 2.1$. κ ,

$$\gamma_F^* = A_F + B_F \beta' + C_F \beta'^2 + D_F \beta' \kappa' + E_F \kappa' + F_F \kappa'^2, \quad (25)$$

$$\gamma_G^* = A_G + B_G \beta' + C_G \beta'^2 + D_G \beta' \kappa' + E_G \kappa' + F_G \kappa'^2, \quad (26)$$

where $\beta' = \beta - 2.0$ and $\kappa' = \kappa - 0.12$. For $\gamma_F^*(PS)$ and $\gamma_G^*(PS)$, we find

$$\begin{aligned} A_F &= 1.9097(41), & B_F &= 0.746(38), \\ C_F &= 0.04(25), & D_F &= -13.9(4.1), \\ E_F &= 20.14(75), & F_F &= -1.(83.), \\ A_G &= 1.8210(28), & B_G &= 0.435(22), \\ C_G &= -0.24(17), & D_G &= 3.2(2.9), \\ E_G &= -1.69(44), & F_G &= -69.(57.), \end{aligned} \quad (27)$$

with $\chi^2/N_{df} = 38.0/17$ and $\chi^2/N_{df} = 19.2/17$, and, for $\gamma_F^*(V)$ and $\gamma_G^*(V)$,

$$A_F = 1.8434(48), \quad B_F = 1.204(46),$$

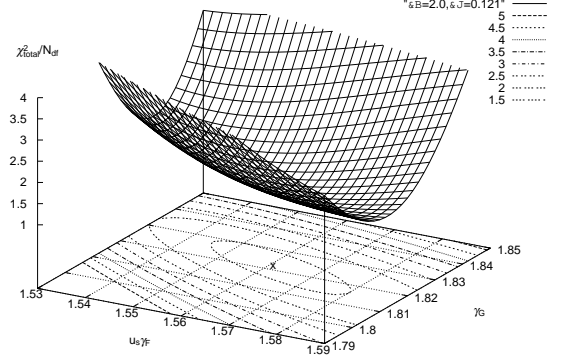


FIG. 10: χ_{total}^2/N_{df} for $\xi = 2$ fits at $\beta = 2.0$ and $\kappa = 0.121$. Results using $\xi_F(PS)$ for the fermionic anisotropy are shown. The minimum of χ_{total}^2/N_{df} is 1.348 at $(u_s \gamma_F, \gamma_G) = (1.5605, 1.8225)$. Curves on the base plane is a contour map of χ_{total}^2/N_{df} . The minimum point is marked by “x” on the contour map. [Note that N_{df} is larger than that for the fits (23) and (24) summarized in Table II because a_F and a_G are not free in this calculation.]

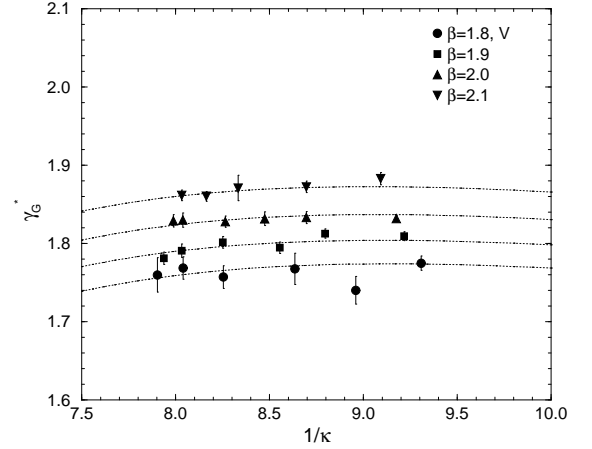
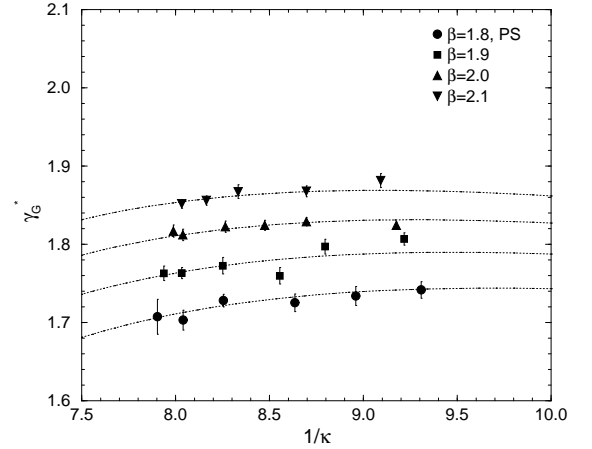


FIG. 11: $\gamma_G^*(PS)$ and $\gamma_G^*(V)$ corresponding to $\xi = 2$. Curves are the results of the global fit (26) with parameters (28) and (30).

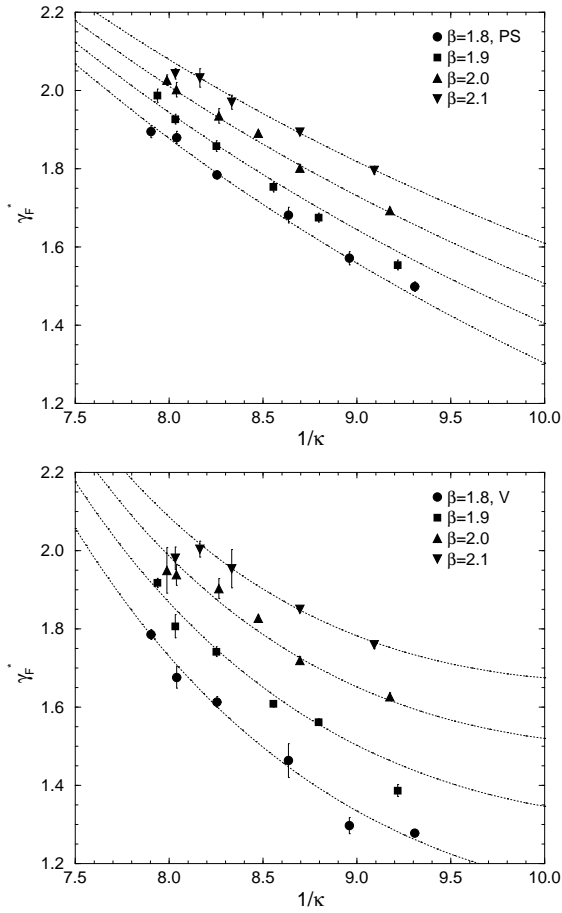


FIG. 12: $\gamma_F^*(\text{PS})$ and $\gamma_F^*(\text{V})$ corresponding to $\xi = 2$. Curves are the results of the global fit (25) with parameters (27) and (29).

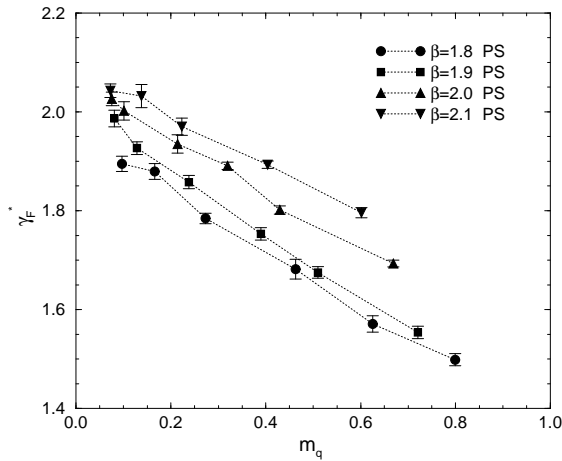


FIG. 13: $\gamma_F^*(\text{PS})$ vs quark mass at various β . Lines are guide of the eyes.

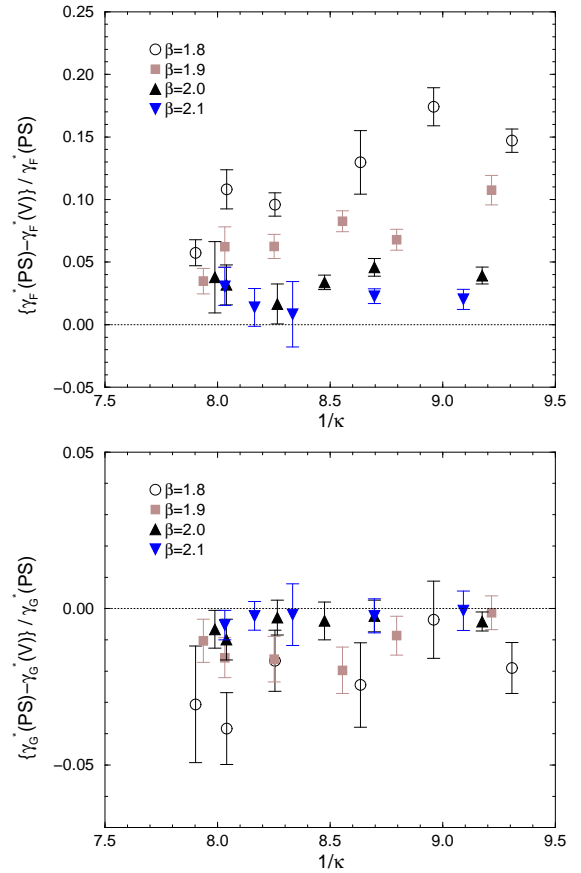


FIG. 14: Relative differences between $\gamma_F^*(\text{PS})$ and $\gamma_F^*(\text{V})$, and between $\gamma_G^*(\text{PS})$ and $\gamma_G^*(\text{V})$, as functions of β and $1/\kappa$.

$$\begin{aligned}
 C_F &= -0.93(29), & D_F &= -21.9(4.7), \\
 E_F &= 25.94(97), & F_F &= 488.(92.), \\
 A_G &= 1.8311(29), & B_G &= 0.348(22), \\
 C_G &= 0.14(20), & D_G &= 0.5(2.9), \\
 E_G &= -1.19(47), & F_G &= -61.(58.),
 \end{aligned} \tag{29}$$

$$\tag{30}$$

with $\chi^2/N_{df} = 76.0/17$ and $\chi^2/N_{df} = 14.6/17$, using the values of $\gamma_{F/G}^*$ and their errors listed in Table. II. The errors for the coefficients are estimated from the χ^2 error matrix. These fits are shown in Figs. 11 and 12 by dotted lines.

In Fig. 13, we plot γ_F^* as a function of the dimensionless quark mass $m_q = (1/\kappa - 1/\kappa_c)/2$ using κ_c determined in Sec. VI. Although the range of m_q is not quite close to the chiral limit, our values of γ_F^* suggest a strong linear dependence in m_q . This result is in clear contrast to the case of quenched QCD in which γ_F^* is well fitted by a quadratic ansatz in m_q motivated from a tree level expression of γ_F^* [30]. As mentioned in Sec. II B, we expect linear corrections from higher order quark loops even if the linear terms are removed at tree level [29]. Our result provides us with an example which confirms this expectation.

Finally, we study the $O(a)$ differences among the cal-

ibration results using PS and V mesons. We plot relative differences between $\gamma_F^*(\text{PS})$ and $\gamma_F^*(\text{V})$, and between $\gamma_G^*(\text{PS})$ and $\gamma_G^*(\text{V})$, in Fig. 14 as functions of β and $1/\kappa$. Errors are estimated neglecting the correlation between PS and V determinations. We find that the differences tend to vanish as β is increased. At $\beta \geq 2.0$, the differences are less than 5% for γ_F^* and 1% for γ_G^* .

VI. PHYSICAL QUANTITIES AT $\xi = 2$

In this section, we interpolate the measurement results to the calibration points corresponding to $\xi = 2$ to estimate the scale and several other basic properties of our lattice. We also test the effects of the two calibration results using PS and V meson dispersion relations on the continuum extrapolation of physical quantities.

For the interpolations to (γ_F^*, γ_G^*) at each (β, κ) , we adopt a linear ansatz

$$y = a + b\gamma_G + c\gamma_F \quad (31)$$

when the range of γ_F is less than 0.3. When $\max(\gamma_F) - \min(\gamma_F) \geq 0.3$, we adopt a quadratic ansatz

$$y = a + b\gamma_G + c\gamma_F + d\gamma_F^2, \quad (32)$$

because, in this case, the linear ansatz sometimes fails to explain the data ($\chi^2/N_{df} \sim O(10) - O(100)$). We find that terms quadratic in γ_G do not improve the fits. We confirm that this quadratic ansatz leads to a result consistent with the linear ansatz if $\max(\gamma_F) - \min(\gamma_F) < 0.3$.

Several physical quantities thus interpolated to $\xi = 2$ are summarized in Table. III, where the results from the quadratic ansatz (32) are marked by “*” on κ . The errors are estimated by quadratically averaging over the contributions from the χ^2 error matrix for the fits (31) or (32), and from the errors for γ_F^* and γ_G^* . Results adopting two alternative choices for the $\xi = 2$ point — $\gamma_{F/G}^*(\text{PS})$ from the pseudo-scalar dispersion relation and $\gamma_{F/G}^*(\text{V})$ from the vector dispersion relation — are labeled by (PS) and (V).

A. Plaquette

Figure 15 shows the plaquette expectation values $W_{11}(ss)$ and $W_{11}(st)$ at $\xi = 2$ adopting $\gamma_{F/G}^*(\text{PS})$. Results adopting $\gamma_{F/G}^*(\text{V})$ are similar. As a reference point, plaquette values on an isotropic lattice using the same action are also plotted [2]. Different points at the same β with the same symbol represent the results obtained at different κ .

Numerical results of plaquettes are compared with their 1-loop values at $\xi = 2$, Eqs. (6) and (7), shown by dashed lines in the Figure. For β we adopt the bare value. We find that, as in the case of isotropic lattices, the plaquettes agree with the perturbative calculation within about 10% at this value of β . This confirms our choice of the clover coefficients c_t and c_s to this accuracy.

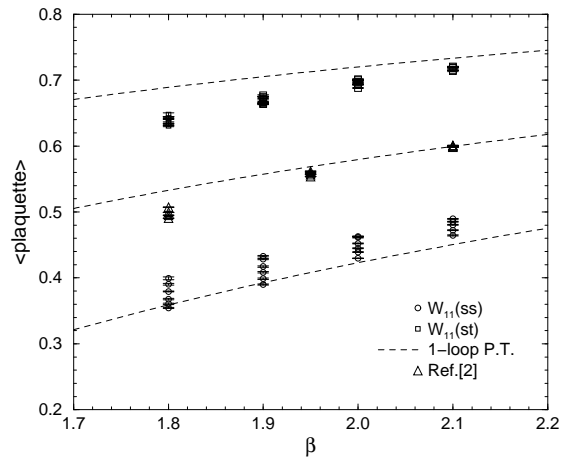


FIG. 15: Plaquettes at $\xi = 2$ and 1. Different points at the same β with the same symbol represent the results obtained at different κ (larger $W_{11}(ss)$ and $W_{11}(st)$ correspond to larger κ). Dashed lines are the results of 1-loop perturbation theory.

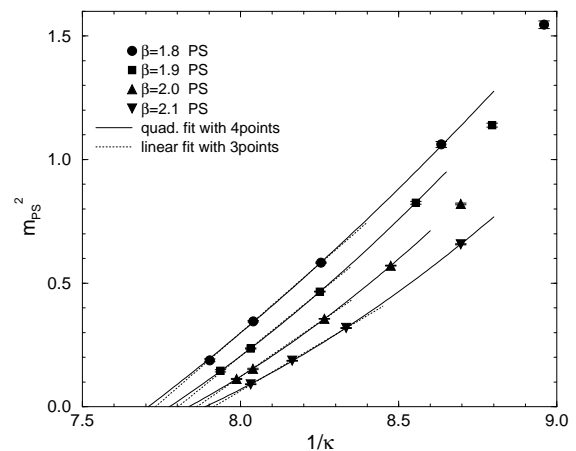


FIG. 16: m_{PS}^2 at $\gamma_{F/G}^*(\text{PS})$ for $\xi = 2$ as a function of $1/\kappa$. Full and dotted curves show quadratic and linear fits using lightest four and three data points, respectively.

B. Light meson spectrum and the lattice scale

In Fig. 16, we summarize the values of m_{PS}^2 at $\xi = 2$ adopting $\gamma_{F/G}^*(\text{PS})$, as a function of $1/\kappa$. Carrying out chiral extrapolations in which the lightest four points are fitted to a quadratic ansatz, we obtain the chiral point $\kappa_c(\text{PS})$ listed in Table IV. The first errors are statistical, while the second ones are systematic errors estimated from the difference with the results of linear fits to the lightest three points. The values of $\kappa_c(\text{V})$ are obtained similarly, adopting $\gamma_{F/G}^*(\text{V})$ as the point for $\xi = 2$. We find that $\kappa_c(\text{PS})$ and $\kappa_c(\text{V})$ are consistent with each other within the present statistical accuracy.

We determine the scale of our lattices from the ρ meson mass $m_\rho = 771.1$ MeV at the physical point $m_{PS}/m_V = m_\pi/m_\rho = 135.0/771.1$. Figure 17 shows m_V

TABLE III: Physical quantities interpolated to $\xi = 2$. Results marked by “*” are from the quadratic ansatz (32), while other results are from the linear ansatz (31). Results of two alternatives for the $\xi = 2$ point, $\gamma_{F/G}^*(\text{PS})$ and $\gamma_{F/G}^*(\text{V})$, are labeled by (PS) and (V), respectively.

β	κ	$m_{PS}(\text{PS})$	χ^2/N_{df}	$m_V(\text{PS})$	χ^2/N_{df}	$m_{PS}/m_V(\text{PS})$	χ^2/N_{df}	$r_0/a_s(\text{PS})$	χ^2/N_{df}
		$m_{PS}(\text{V})$	χ^2/N_{df}	$m_V(\text{V})$	χ^2/N_{df}	$m_{PS}/m_V(\text{V})$	χ^2/N_{df}	$r_0/a_s(\text{V})$	χ^2/N_{df}
1.8	0.10745*	1.4395(66)	8.2/ 4	1.5760(75)	2.6/ 4	0.91339(37)	1.3/ 4	1.299(15)	2.6/ 4
		1.5601(55)	8.2/ 4	1.7178(64)	2.6/ 4	0.90828(43)	1.3/ 4	1.320(19)	2.6/ 4
	0.11162*	1.2431(62)	1.1/ 2	1.3985(75)	3.1/ 2	0.88900(57)	2.8/ 2	1.346(18)	1.5/ 2
		1.3009(39)	1.1/ 2	1.4720(45)	3.1/ 2	0.88382(65)	2.8/ 2	1.355(19)	1.5/ 2
	0.11582	1.0302(57)	7.9/ 3	1.2043(78)	7.1/ 3	0.8556(10)	3.1/ 3	1.413(11)	3.0/ 3
		1.079(12)	7.9/ 3	1.275(17)	7.1/ 3	0.8458(23)	3.1/ 3	1.406(19)	3.0/ 3
	0.12115	0.7635(15)	2.9/ 3	0.9679(25)	5.5/ 3	0.7888(12)	3.0/ 3	1.5210(64)	8.5/ 3
		0.7660(26)	2.9/ 3	0.9906(42)	5.5/ 3	0.7732(19)	3.0/ 3	1.557(12)	8.5/ 3
	0.12438*	0.5880(25)	5.7/ 4	0.8165(36)	7.4/ 4	0.7200(22)	6.1/ 4	1.605(10)	8.1/ 4
		0.5448(73)	5.7/ 4	0.7973(46)	7.4/ 4	0.6834(74)	6.1/ 4	1.701(13)	8.1/ 4
	0.12655	0.4347(71)	9.1/ 3	0.6841(45)	4.3/ 3	0.6356(80)	3.9/ 3	1.730(11)	4.2/ 3
		0.3838(62)	9.1/ 3	0.6627(46)	4.3/ 3	0.5805(70)	3.9/ 3	1.796(10)	4.2/ 3
1.9	0.10850*	1.3255(56)	4.5/ 4	1.4428(65)	2.3/ 4	0.91851(50)	1.5/ 4	1.5015(66)	18.2/ 4
		1.4045(79)	4.5/ 4	1.5330(90)	2.3/ 4	0.91599(54)	1.5/ 4	1.5101(73)	18.2/ 4
	0.11370	1.0672(38)	7.5/ 3	1.2002(46)	5.7/ 3	0.88860(95)	10.3/ 3	1.6041(80)	2.4/ 3
		1.0977(27)	7.5/ 3	1.2393(32)	5.7/ 3	0.88535(59)	10.3/ 3	1.6140(49)	2.4/ 3
	0.11690	0.9085(30)	4.9/ 5	1.0557(42)	8.9/ 5	0.86105(98)	9.4/ 5	1.6376(71)	4.3/ 5
		0.9304(20)	4.9/ 5	1.0891(27)	8.9/ 5	0.85428(61)	9.4/ 5	1.6742(44)	4.3/ 5
	0.12120*	0.6825(15)	5.8/ 4	0.8460(27)	5.7/ 4	0.8066(17)	2.1/ 4	1.795(10)	1.8/ 4
		0.6793(13)	5.8/ 4	0.8516(25)	5.7/ 4	0.7976(18)	2.1/ 4	1.821(10)	1.8/ 4
	0.12450*	0.4859(24)	5.9/ 3	0.6720(21)	0.6/ 3	0.7234(28)	2.7/ 3	1.9708(70)	19.1/ 3
		0.4593(73)	5.9/ 3	0.6599(40)	0.6/ 3	0.6958(81)	2.7/ 3	2.016(18)	19.1/ 3
	0.12600	0.3804(61)	33.6/ 3	0.5839(39)	8.5/ 3	0.6517(79)	10.7/ 3	2.119(14)	1.6/ 3
		0.3559(43)	33.6/ 3	0.5722(30)	8.5/ 3	0.6205(56)	10.7/ 3	2.165(10)	1.6/ 3
2.0	0.10900	1.1913(26)	0.9/ 2	1.2830(30)	1.7/ 2	0.92857(36)	0.6/ 2	1.7792(53)	3.9/ 2
		1.2143(35)	0.9/ 2	1.3097(40)	1.7/ 2	0.92725(39)	0.6/ 2	1.7844(55)	3.9/ 2
	0.11500	0.9057(18)	2.2/ 3	1.0131(24)	6.2/ 3	0.89420(51)	8.3/ 3	1.9326(45)	8.2/ 3
		0.9201(22)	2.2/ 3	1.0323(30)	6.2/ 3	0.89158(69)	8.3/ 3	1.9471(66)	8.2/ 3
	0.11800	0.75539(97)	1.2/ 2	0.8696(14)	0.3/ 2	0.86874(67)	0.4/ 2	2.0380(48)	5.1/ 2
		0.7604(13)	1.2/ 2	0.8778(18)	0.3/ 2	0.86623(92)	0.4/ 2	2.0553(68)	5.1/ 2
	0.12100	0.59609(94)	26.3/ 3	0.7225(14)	14.6/ 3	0.8251(15)	0.6/ 3	2.229(11)	1.5/ 3
		0.59505(95)	26.3/ 3	0.7231(15)	14.6/ 3	0.8229(19)	0.6/ 3	2.241(11)	1.5/ 3
	0.12440	0.3912(35)	11.5/ 6	0.5397(23)	20.9/ 6	0.7254(41)	11.6/ 6	2.527(13)	14.6/ 6
		0.3784(50)	11.5/ 6	0.5319(31)	20.9/ 6	0.7116(57)	11.6/ 6	2.570(18)	14.6/ 6
	0.12520	0.3355(37)	8.5/ 2	0.4906(28)	5.6/ 2	0.6843(56)	0.1/ 2	2.599(16)	0.3/ 2
		0.315(15)	8.5/ 2	0.4819(67)	5.6/ 2	0.655(23)	0.1/ 2	2.660(47)	0.3/ 2
2.1	0.11000	1.0442(32)	3.2/ 1	1.1150(36)	0.2/ 1	0.93648(52)	3.4/ 1	2.2324(72)	13.1/ 1
		1.0545(32)	3.2/ 1	1.1264(36)	0.2/ 1	0.93610(47)	3.4/ 1	2.2372(61)	13.1/ 1
	0.11500	0.8108(13)	9.0/ 2	0.8898(16)	4.8/ 2	0.91143(49)	0.0/ 2	2.4000(63)	1.5/ 2
		0.8162(14)	9.0/ 2	0.8963(17)	4.8/ 2	0.91097(59)	0.0/ 2	2.4134(68)	1.5/ 2
	0.12000	0.56448(90)	1.3/ 2	0.6577(14)	1.3/ 2	0.8584(11)	0.5/ 2	2.6992(94)	0.3/ 2
		0.5644(14)	1.3/ 2	0.6582(24)	1.3/ 2	0.8577(20)	0.5/ 2	2.705(18)	0.3/ 2
	0.12250	0.4313(14)	5.8/ 3	0.5339(12)	3.6/ 3	0.8075(28)	5.3/ 3	2.875(10)	10.0/ 3
		0.4294(13)	5.8/ 3	0.5335(13)	3.6/ 3	0.8044(25)	5.3/ 3	2.881(11)	10.0/ 3
	0.12450	0.3015(23)	10.4/ 2	0.4220(19)	11.9/ 2	0.7134(32)	7.9/ 2	3.177(15)	1.6/ 2
		0.2906(48)	10.4/ 2	0.4149(34)	11.9/ 2	0.6997(63)	7.9/ 2	3.229(27)	1.6/ 2

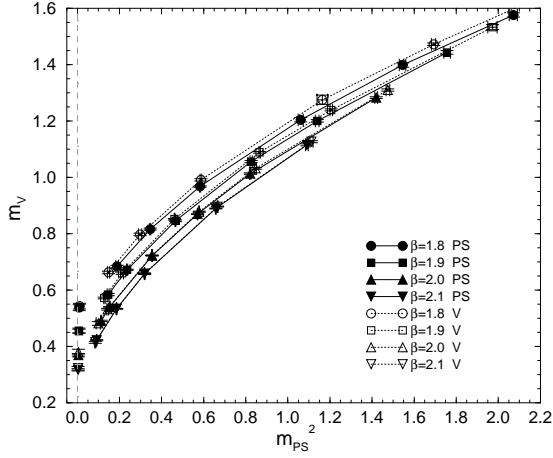


FIG. 17: m_V as a function of m_{PS}^2 for $\xi = 2$ at $\gamma_{F/G}^*$ (PS) (filled symbols) and at $\gamma_{F/G}^*$ (V) (open symbols). The leftmost symbols are the results of quadratic extrapolations to the physical point. The lines are guide for the eyes.

TABLE IV: Critical hopping parameter κ_c . The numbers in the first bracket are statistical errors, and those in the second bracket are systematic errors from the chiral extrapolation.

β	$1/\kappa_c(\text{PS})$	$1/\kappa_c(\text{V})$
1.8	$7.708(43)(^{+23}_{-0})$	$7.763(80)(^{+25}_{-0})$
1.9	$7.775(39)(^{+27}_{-0})$	$7.789(46)(^{+30}_{-0})$
2.0	$7.836(26)(^{+25}_{-0})$	$7.862(50)(^{+22}_{-0})$
2.1	$7.888(14)(^{+27}_{-0})$	$7.896(24)(^{+31}_{-0})$

as a function of m_{PS}^2 at $\gamma_{F/G}^*$ (PS) and $\gamma_{F/G}^*$ (V). We find that the masses at $\gamma_{F/G}^*$ (PS) and $\gamma_{F/G}^*$ (V) are slightly different on coarse lattices. The difference rapidly decreases with increasing β .

Extrapolation to the physical point is done adopting a quadratic ansatz to the lightest four data points at each β . We note that, with the present statistics, two results of m_V at $\gamma_{F/G}^*$ (PS) and $\gamma_{F/G}^*$ (V), extrapolated to the physical point, are consistent with each other already on the coarsest lattice. High statistics simulations directly at $\gamma_{F/G}^*$ (PS) and $\gamma_{F/G}^*$ (V) may resolve the difference at the physical point.

The resulting lattice scale is summarized in Table V.

TABLE V: Lattice scale determined from m_ρ at the physical point.

β	$a_s(\text{PS}) [\text{GeV}^{-1}]$	$a_s(\text{V}) [\text{GeV}^{-1}]$	$L_s a_s [\text{fm}]$
1.8	$1.395(28)(^{+95}_{-0})$	$1.408(26)(^{+67}_{-0})$	2.2
1.9	$1.185(21)(^{+80}_{-0})$	$1.178(17)(^{+55}_{-0})$	1.9
2.0	$0.957(15)(^{+68}_{-0})$	$0.986(26)(^{+61}_{-0})$	1.9
2.1	$0.824(10)(^{+62}_{-0})$	$0.838(17)(^{+70}_{-0})$	2.0

TABLE VI: Parameters for the calculation of the static quark potential.

β	κ	n_{smear}	fit-range in t	fit-range in r
1.8	0.10745 – 0.11582	1	3 – 6	$\sqrt{2} - 2\sqrt{3}$
	0.12115 – 0.12655	1	3 – 6	$\sqrt{2} - 3\sqrt{2}$
1.9	0.1085 – 0.1169	2	3 – 6	$\sqrt{2} - 3\sqrt{2}$
	0.1212 – 0.1260	2	4 – 7	$\sqrt{2} - 3\sqrt{3}$
2.0	0.1090 – 0.1180	3	4 – 7	$\sqrt{2} - 3\sqrt{3}$
	0.1210 – 0.1252	3	5 – 9	$\sqrt{3} - 6.0$
2.1	0.1100 – 0.1200	4	5 – 9	$\sqrt{3} - 6.0$
	0.1225 – 0.1245	4	6 – 11	$2.0 - 3\sqrt{6}$

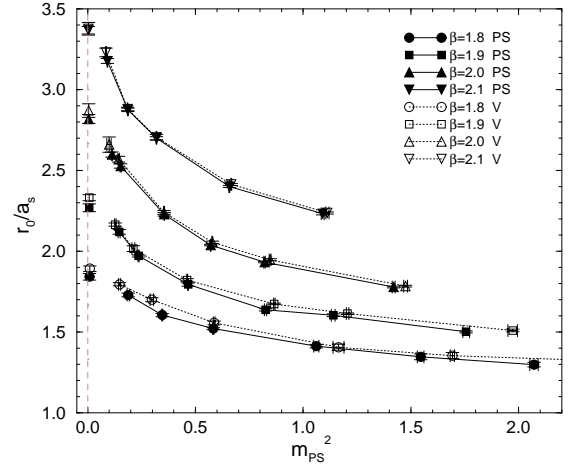


FIG. 18: Sommer scale at $\xi = 2$ as a function of the PS meson mass. The leftmost symbols are the results of quadratic extrapolations to the physical point. The lines are guide for the eyes.

Systematic errors (second errors) in the table are estimated from a comparison with linear fits using the lightest three points.

C. Static quark potential and Sommer scale

We extract the static quark potential $V(r)$ from a fit

$$W(r, t) = C(r) \exp[-V(r)t], \quad (33)$$

TABLE VII: Sommer scale at $\xi = 2$, extrapolated to the physical point.

β	$r_0/a_s(\text{PS})$	$r_0/a_s(\text{V})$
1.8	$1.843(21)(^{+0}_{-47})$	$1.892(17)(^{+0}_{-26})$
1.9	$2.269(23)(^{+0}_{-77})$	$2.331(18)(^{+0}_{-56})$
2.0	$2.818(27)(^{+0}_{-62})$	$2.870(41)(^{+0}_{-78})$
2.1	$3.367(23)(^{+0}_{-91})$	$3.377(39)(^{+0}_{-118})$

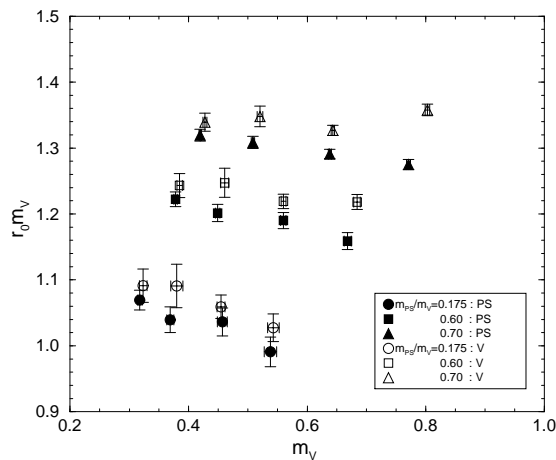


FIG. 19: Sommer scale at $m_{PS}/m_V = 0.7, 0.6$ and 0.175 (the physical point) as a function of the lattice spacing. Errors are statistical.

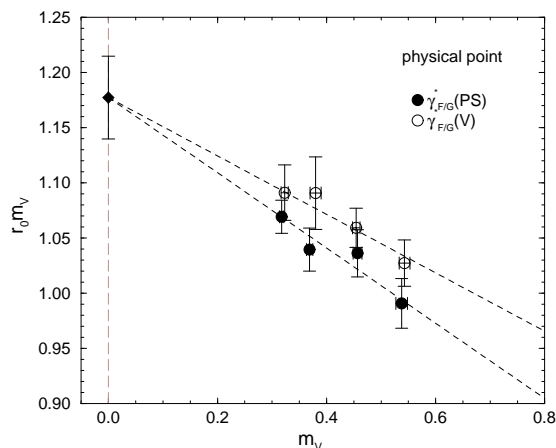


FIG. 20: Sommer scale at the physical point as a function of the lattice spacing. Errors are statistical. Lines show the continuum extrapolation with a constraint requiring the same continuum value for PS and V results.

to temporal Wilson loops. In order to enhance the overlap $C(r)$ with the ground state, we smear spatial links [31]. We fit the data at $t \approx 0.45 - 0.90$ fm where a large overlap is observed. As in previous studies on isotropic lattices, we find no apparent string breaking effects in $V(r)$. Therefore, we fit the potential with

$$V(r) = A + \frac{\alpha}{r} + \sigma r. \quad (34)$$

for the range $r \approx 0.35 - 1.5$ fm. Parameters for the potential calculations are summarized in Table VI.

With (34), the Sommer scale r_0 [32] defined by

$$r_0^2 \frac{dV(r)}{dr} \Big|_{r=r_0} = 1.65 \quad (35)$$

is given by

$$\frac{r_0}{a_s} = \sqrt{\frac{1.65 + \alpha\xi}{\sigma\xi}}. \quad (36)$$

Results of r_0/a_s interpolated to $\xi = 2$ are listed in Table III and shown in Fig. 18. Extrapolating to the physical point, we obtain the values summarized in Table VII, where the central values are from quadratic fits in m_{PS}^2 using the lightest four κ 's and the systematic errors are estimated from the difference with a linear fit using the lightest three κ 's.

The Sommer scale at $m_{PS}/m_V = 0.7, 0.6$ and 0.175 (the physical point) from a quadratic fit is plotted in Fig. 19 as a function of the lattice spacing. We find that the difference between the calibrations using the PS and V meson dispersion relations becomes smaller toward the continuum limit. For the Sommer scale at the physical point, a naive linear extrapolation to the continuum limit gives $r_0 = 0.597(24)_{(-14)}^{(+52)}$ and $0.612(33)_{(-37)}^{(+79)}$ fm for $\gamma_{F/G}^*$ using the PS and V meson dispersion relations, respectively. The systematic errors are estimated comparing the results of various combinations of chiral extrapolations (linear and quadratic fits for m_V and r_0). We find that the results using $\gamma_{F/G}^*(PS)$ and $\gamma_{F/G}^*(V)$ are consistent in the continuum limit within the statistical errors. A constrained fit requiring the same continuum value, as shown in Fig. 20, leads to $r_0 = 0.603(19)_{(-22)}^{(+60)}$ fm, where the statistical error was estimated neglecting the correlation between the PS and V results and the systematic error was estimated from the results of constrained fits using various combinations of chiral extrapolations for m_V and r_0 .

D. Beta functions

Finally we attempt a rough estimation of beta functions

$$a_s \frac{\partial \kappa}{\partial a_s} \Big|_{\frac{m_{PS}}{m_V}}, \quad a_s \frac{\partial \beta}{\partial a_s} \Big|_{\frac{m_{PS}}{m_V}} \quad (37)$$

along lines of constant physics defined by $m_{PS}/m_V = \text{constant}$. These quantities are required in a calculation of the equation of state in thermal QCD [20]. We calculate the beta functions by

$$\begin{aligned} & \left(\begin{array}{cc} \frac{\partial \beta}{\partial(m_V a_t)} & \frac{\partial \kappa}{\partial(m_V a_t)} \\ \frac{\partial \beta}{\partial(m_{PS}/m_V)} & \frac{\partial \kappa}{\partial(m_{PS}/m_V)} \end{array} \right) \\ & = \left(\begin{array}{cc} \frac{\partial(m_V a_t)}{\partial \beta} & \frac{\partial(m_{PS}/m_V)}{\partial \beta} \\ \frac{\partial(m_V a_t)}{\partial \kappa} & \frac{\partial(m_{PS}/m_V)}{\partial \kappa} \end{array} \right)^{-1} \end{aligned} \quad (38)$$

using the data for m_{PS} and m_V listed in Table III. In Ref. [20], a slightly different method was adopted because the matrix in the right hand side of (38) sometimes becomes almost singular in the large quark mass region.

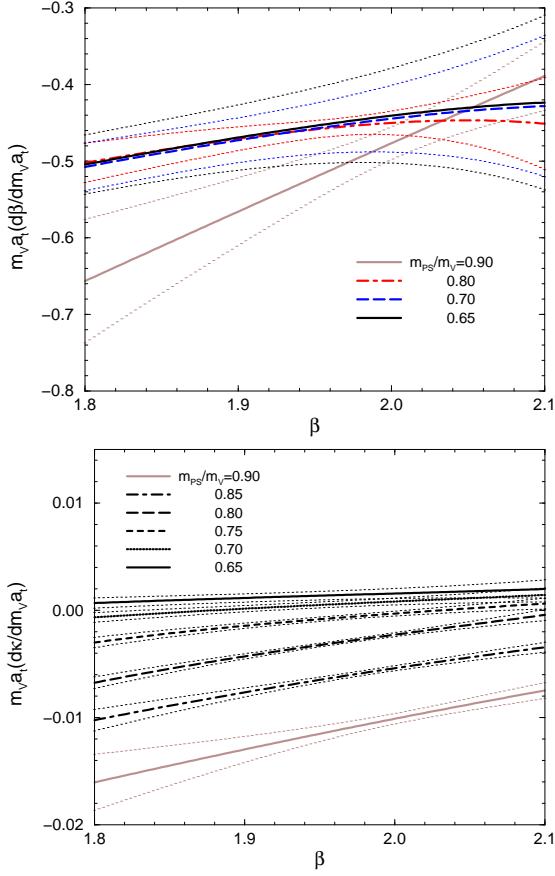


FIG. 21: Beta functions (37) at $\gamma_{F/G}^*(PS)$ for $\xi = 2$. Thick curves are the results for given values of m_{PS}/m_V , while thin curves represent their errors.

Since quarks are not quite heavy in this study, we adopt the simpler method using (38). We fit m_{PS} and m_V to the general quadratic ansatz in β and κ . Because the data noticeably deviates from the quadratic form when we include all values of κ , we restrict ourselves to three κ 's around the target m_{PS}/m_V in the fit, while all four β 's are included. Our estimates for the beta functions are summarized in Figs. 21 and 22.

VII. CONCLUSIONS

In this article we initiated a systematic study of two-flavor full QCD on anisotropic lattices. We have determined, for the clover-improved Wilson quarks coupled to an RG-improved glue, the bare anisotropy parameters which realize a consistent renormalized anisotropy $\xi = 2$ in both quark and gauge sectors. In the quark sector we employed both pseudo scalar and vector meson channels for calibration. The results for the bare anisotropy parameters are summarized in Eqs. (25)–(30) as functions of β and κ for the range $a_s \approx 0.28$ – 0.16 fm and $m_{PS}/m_V \approx 0.6$ – 0.9 . The difference between the two

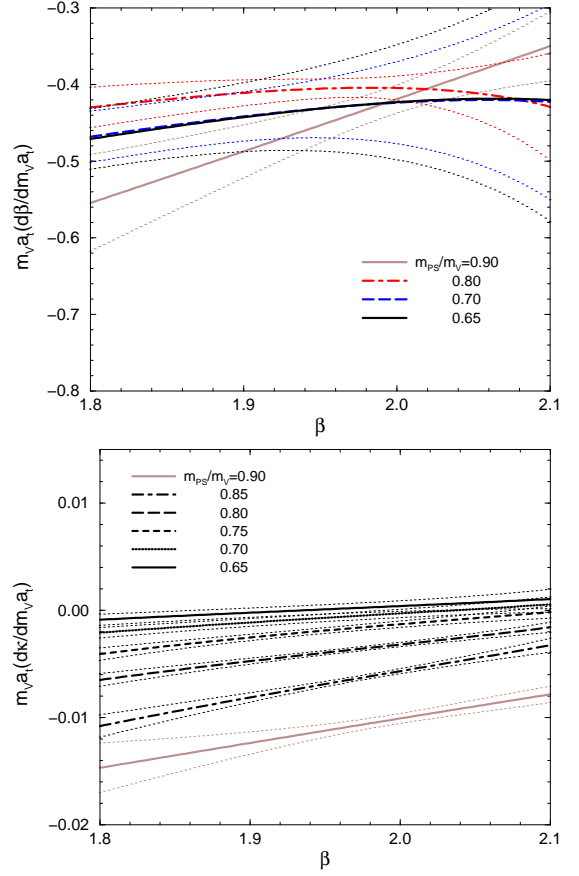


FIG. 22: Same as Fig. 21 but at $\gamma_{F/G}^*(V)$.

calibration methods should be $O(a)$. We confirmed that the difference in the bare anisotropy parameters actually vanishes toward the continuum limit.

We have also attempted to calculate some basic quantities using data measured in the runs made for the calibration and interpolating them to the point corresponding to $\xi = 2$. Although errors from interpolations are introduced, this enabled us to carry out an initial determination of the lattice scale and beta functions. For the Sommer scale r_0 , we found that r_0 from different calibration methods led to a consistent value in the continuum limit.

We wish to apply our results to study of heavy quarks and thermal QCD, in which simulations can be directly made with $\xi = 2$ anisotropic lattices using the parametrizations Eqs. (25)–(30). We hope to report on such studies in the near future.

This work is in part supported by the Large-Scale Numerical Simulation Project of the Science Information Processing Center (S.I.P.C) of the University of Tsukuba and by the Grants-in-Aid for Scientific Research by the ministry of Education (Nos. 12304011, 12640253, 12740133, 13640259, 13640260, 13135204, 14046202, 11640294). Simulations are carried out on Fu-

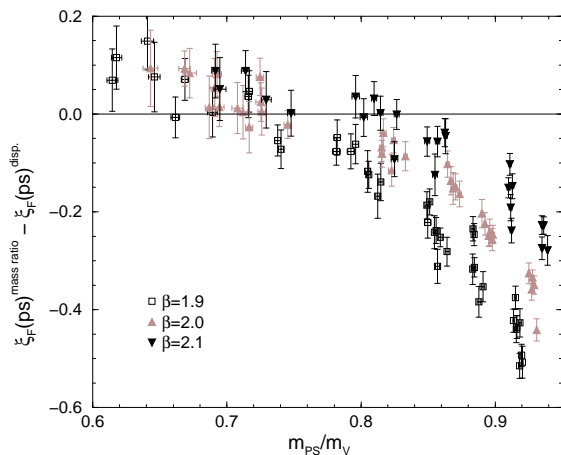


FIG. 23: $\xi_F^{\text{mass ratio}}(\text{PS}) - \xi_F^{\text{disp.}}(\text{PS})$ as a function of m_{PS}/m_V at various values of β and κ .

jitsu VPP5000 at S.I.P.C.

Appendix A: ξ_F from the ratio of screening and temporal masses

In this paper, we adopt the dispersion relation for mesons for defining the fermionic anisotropy ξ_F . An alternative definition of ξ_F is given by the ratio of the masses measures in a spatial direction (screening mass m_s) and the temporal direction (temporal mass m_t),

$$\xi_F^{\text{mass ratio}} = m_s/m_t, \quad (39)$$

as adopted in a quenched study for PS mesons [5]. For clarity, we denote ξ_F defined by (18) using the dispersion

relation as $\xi_F^{\text{disp.}}$ in this appendix.

A disadvantage of the mass ratio method is that, to obtain reliable values of m_s and m_t suppressing contamination of excited states, we need to prepare well-tuned smeared sources both in the spatial and temporal directions, and/or carry out multi-pole fits, on sufficiently large lattices. In this paper, because we do not have propagators with temporally smeared sources, we study spatial propagators with point-point source and sink. We find that, when quarks are light, the effective mass of the spatial PS meson correlator does not show a clear plateau, and sometimes shows a decreasing tendency even at the maximum distance $x = N_s/2 - 1$. This means that our spatial lattice sizes 8–12 may not be large enough to suppress excited states. Unfortunately, the number of data points is also not sufficient to attempt a multi-pole fit. Therefore, in the following, we just adopt the value of effective mass at $x = N_s/2 - 1$ for m_s . Strictly speaking, this value gives an upper bound of m_s . Therefore, the resulting $\xi_F^{\text{mass ratio}}$ may be larger than the true value when quarks are light.

Because our temporal lattice sizes are sufficiently large, we do not encounter a similar problem in the calculations of m_t and $\xi_F^{\text{disp.}}$.

Figure 23 shows the difference of the two fermionic anisotropies $\xi_F^{\text{mass ratio}}(\text{PS}) - \xi_F^{\text{disp.}}(\text{PS})$ as a function of m_{PS}/m_V at $\beta = 1.9, 2.0$ and 2.1 . We find that the difference is consistent with zero when m_{PS}/m_V is small. A slight overshooting at $m_{PS}/m_V \lesssim 0.7$ may be understood by the fact that our $\xi_F^{\text{mass ratio}}$ is an upper bound for the true value as discussed above. We also find that the difference at large quark masses decreases toward the continuum limit. At $\beta \gtrsim 2.0$ (2.1), two methods are consistent with each other at $m_{PS}/m_V \lesssim 0.75$ (0.8).

-
- [1] A. Ali Khan *et al.* (CP-PACS Collaboration), Phys. Rev. Lett. 85 (2000) 4674.
[2] A. Ali Khan *et al.* (CP-PACS Collaboration), Phys. Rev. D65 (2002) 054505.
[3] Y. Namekawa *et al.* (CP-PACS Collaboration), Phys. Rev. D64 (2001) 074507.
[4] S. Sakai, T. Saito and A. Nakamura, Nucl. Phys. B584 (2000) 528.
[5] Ph. de Forcrand *et al.* (QCD-TARO Collaboration), Phys. Rev. D63 (2001) 054501.
[6] T. Umeda *et al.*, Int. J. Mod. Phys. A16 (2001) 2215.
[7] N. Ishii, H. Sukanuma and H. Matsufuru, Phys. Rev. D66 (2002) 094506.
[8] M. Asakawa, T. Hatsuda, Y. Nakahara, hep-lat/0208059.
[9] T. Umeda, K. Nomura and H. Matsufuru : hep-lat/0211003
[10] T.R. Klassen, Nucl. Phys. B533 (1998) 557.
[11] P. Chen, Phys. Rev. D64 (2001) 034509.
[12] M. Okamoto *et al.* (CP-PACS Collaboration), Phys. Rev. D65 (2002) 094508.
[13] T. Manke *et al.* (CP-PACS Collaboration), Phys. Rev. Lett. 82 (1999) 4396.
[14] J. Harada *et al.*, Phys. Rev. D66 (2002) 014509.
[15] C.J. Morningstar and M. Peardon, Phys. Rev. D60 (1999) 034509.
[16] C. Liu *et al.*, Nucl. Phys. B624 (2002) 360.
[17] T. Hashimoto, A. Nakamura and I.O. Stamatescu, Nucl. Phys. B406 (1993) 325.
[18] A. Ali Khan *et al.* (CP-PACS Collaboration), Phys. Rev. D63 (2000) 034502.
[19] A. Ali Khan *et al.* (CP-PACS Collaboration), Phys. Rev. D64 (2001) 054504.
[20] A. Ali Khan *et al.* (CP-PACS Collaboration), Phys. Rev. D64 (2001) 074510.
[21] A. Ali Khan *et al.* (CP-PACS Collaboration), Phys. Rev. D64 (2001) 114501.
[22] V.I. Lesk *et al.* (CP-PACS Collaboration), hep-lat/0211040.

- [23] S. Aoki *et al.* (CP-PACS Collaboration), Phys. Rev. D60 (1999) 114508.
- [24] Y. Iwasaki, K. Kanaya, S. Kaya, and T. Yoshié, Phys. Rev. Lett. 78 (1997) 179.
- [25] Y. Iwasaki, Nucl. Phys. B258 (1985) 141; Univ. of Tsukuba report UTHEP-118 (1983), unpublished.
- [26] S. Ejiri, K. Kanaya, Y. Namekawa and T. Umeda, hep-lat/0301029.
- [27] B. Sheikholeslami and R. Wohlert, Nucl. Phys. B259 (1985) 572.
- [28] J. Harada *et al.*, Phys. Rev. D64 (2001) 074501.
- [29] S. Aoki, Y. Kuramashi and S. Tominaga, hep-lat/0107009; Nucl. Phys. B (Proc. Suppl.) 106 (2002) 349.
- [30] H. Matsufuru, T. Onogi and T. Umeda, Phys. Rev. D64 (2001) 114503.
- [31] G.S. Bali and K. Schilling, Phys. Rev. D46 (1992) 2636, G.S. Bali, C. Schlichter and K. Schilling, Phys. Rev. D51 (1995) 5165.
- [32] R. Sommer, Nucl. Phys. B411 (1994) 839.